



Attached and separated rotating flow over a finite height ridgeS. Frei **Department of Mathematics and Statistics, University of Konstanz, Universitätsstraße 10,
78457 Konstanz, Germany*E. Burman † and E. Johnson ‡*Department of Mathematics, University College London, United Kingdom*

(Received 27 February 2024; accepted 11 July 2024; published 2 August 2024)

This article discusses the effect of rotation on the boundary layer in high Reynolds number flow over a ridge using a numerical method based on stabilized finite elements that captures steady solutions up to a Reynolds number of order 10^6 . The results are validated against boundary layer computations in shallow flows and for deep flows against experimental observations reported in Machicoane *et al.* [[Phys. Rev. Fluids 3, 034801 \(2018\)](#)]. In all cases considered the boundary layer remains attached, even at arbitrarily large Reynolds numbers, provided the Rossby number of the flow is less than some critical Rossby number of order unity. At any fixed Rossby number larger than this critical value, the flow detaches at sufficiently high Reynolds number to form a steady recirculating region in the lee of the ridge. At even higher Reynolds numbers no steady flow is found. This disappearance of steady solutions closely reproduces the transition to unsteadiness seen in the laboratory.

DOI: [10.1103/PhysRevFluids.9.084801](https://doi.org/10.1103/PhysRevFluids.9.084801)**I. INTRODUCTION**

Mason and Sykes [1] observe that topography with horizontal length scales of the order of a few kilometers is often sufficiently steep to induce flow separation in the atmosphere and that such flows might be expected to produce significant changes in the momentum exchange between the atmosphere and the surface. In addition to exerting a form drag on the fluid, separated flow over topography leads to enhanced mixing in the lee of the topography, affecting the lee-wave field and may make a significant contribution to the overall vertical mixing in the region [2]. More recently, Machicoane *et al.* [3] present theoretical and experimental results for flow past a horizontal cylinder in horizontal motion relative to a frame rotating rapidly about a vertical axis. Their work discusses in detail the inertial lee-wave field generated by the cylinder, significantly extending the results of [4], and also includes a discussion of experimental results for the onset, with increasing translation speed of the cylinder, of separation and subsequent unsteadiness in the flow. They note that rotation strongly suppresses separation and suggest, from the experimental results, that with increasing flow speed the flow changes directly from being steady and attached to being unsteady and detached as the product of the Rossby and Reynolds numbers ($Ro = U^*/2\Omega L$, $Re = U^*L/\nu$ for flow speed U^* , rotation rate Ω , kinematic viscosity ν , and typical horizontal scale L) for the flow passes through 275 ± 25 . This contrasts with nonrotating flow where separation occurs at $Re \approx 3$ but wake

*Contact author: stefan.frei@uni-konstanz.de†Contact author: e.burman@ucl.ac.uk‡Contact author: e.johnson@ucl.ac.uk

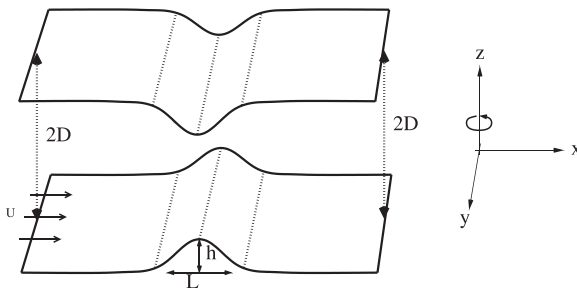


FIG. 1. The flow geometry. A ridge of dimensional height h and width L lies on the floor $z^* = 0$ of a domain of unperturbed depth $2D$ with a complementary ridge on the upper boundary. The domain rotates around the vertical z^* axis with angular velocity Ω and the oncoming flow has constant horizontal velocity U^* (outside boundary layers) perpendicular to the ridge crest.

instability at $\text{Re} \approx 47$ [3,5]. The purpose of the present work is to examine this lee separation in rotating flows in greater detail.

To obtain the critical Reynolds numbers for this nonlinear flow over a wide range of Rossby numbers requires a stable numerical method which is robust independently of the Reynolds number. We employ a stabilized equal-order finite-element method using *Continuous Interior Penalty stabilization*, going back to Douglas and Dupont [6]. The method was first used in fluid flow problems by Burman, Hansbo, and Fernández for the Stokes, Darcy, and Oseen equations [7,8] and later for more complex problems, such as flows at high Reynolds numbers [9], including turbulent flows [10], as well as fluid-structure interactions [11,12].

The structure of this article is as follows. Section II introduces the geometry and the governing equations. Section III introduces a streamfunction formulation for finite height ridges and obtains the outer and inner (boundary layer) solutions at large Reynolds number for shallow flow. The numerical method for the boundary-layer solution is given in the Appendix. Section IV introduces the numerical method, showing that for attached flow the results for increasing Reynolds number converge towards the boundary layer solutions, but also capture steady separated flows at larger Rossby numbers. Section V extends the results to deep flow allowing inertial waves to appear in the outer flow but showing the same qualitative behavior of separation and unsteadiness as shallow flows. Section VI investigates deep rotating flow over a horizontal cylinder, the geometry of Machicoane *et al.* [3], and shows that the numerical simulations capture much of the experimental observations. Section VII gives brief conclusions.

II. GOVERNING EQUATIONS

Consider a fluid of constant density ρ and kinematic viscosity ν in solid body rotation about a vertical axis at angular velocity Ω . Introduce Cartesian axes $Ox^*y^*z^*$ fixed in the fluid with Oz^* vertical. Let the fluid lie above a horizontal boundary perturbed by a ridge of height h and horizontal scale L , given by $z^* = hb(x^*/L)$, where the function b gives the ridge profile and has a maximum value unity. Let the fluid be bounded above at height $z^* = 2D$ by a horizontal boundary perturbed downwards by a complementary ridge so that the flow geometry is symmetric about the line $z^* = D$ and the motion has aspect ratio $\delta = D/L$ (Fig. 1).

Now suppose the fluid is set in steady motion, relative to the rotating frame, so that at large distance, outside viscous layers on the boundaries, the flow is uniform with constant speed U^* in the positive x^* direction. The Coriolis force associated with this uniform flow is balanced by a constant pressure gradient of magnitude $2\rho\Omega U$ in the negative y^* direction. In the absence of the ridge ($h = 0$), and far upstream of the ridge when $h > 0$, the flow is the usual Ekman layer flow with boundary layers of thickness $(\nu/\Omega)^{1/2}$ on the upper and lower boundaries. The flow is independent

of the coordinate y^* and so nondimensionalizing lengths on L , velocities on U^* and the pressure on ρU^{*2} gives the two-dimensional governing equations

$$uu_x + wu_z - \text{Ro}^{-1}v = -p_x + \text{Re}^{-1}\nabla^2u, \quad (1a)$$

$$uv_x + wv_z + \text{Ro}^{-1}(u - 1) = \text{Re}^{-1}\nabla^2v, \quad (1b)$$

$$uw_x + ww_z = -p_z + \text{Re}^{-1}\nabla^2w, \quad (1c)$$

$$u_x + w_z = 0, \quad (1d)$$

with the constant in (1b) giving the constant far-field pressure gradient in the y direction. On the top and bottom boundaries the flow satisfies the viscous boundary conditions that the velocity vanishes, i.e., $u = v = w = 0$. The two nondimensional parameters appearing are the Reynolds number $\text{Re} = UL/\nu$, measuring the ratio of inertial to viscous forces, and the Rossby number $\text{Ro} = U/2\Omega L$, measuring the ratio of inertial to Coriolis forces. Since the nonlinear inertial terms are always significant in the flows discussed below, Re and Ro are taken, together with the aspect ratio δ , as the fundamental parameters. The Ekman number $E = \nu/2\Omega D^2 = \text{Ro}/\delta^2\text{Re}$ appears naturally with $E^{1/2}$ measuring the ratio of the Ekman layer thickness to the fluid depth and is treated as derived from the fundamental parameters.

Integrating (1d) across the fluid depth gives the dimensional result

$$\int u^* dz^* = 2U^*D, \quad (2)$$

showing the mass flux per unit width in the y direction is constant and equal to its upstream value. The dimensional form of (1b), outside boundary layers, can be written

$$(u^*v^*)_{x^*} + (w^*v^*)_{z^*} = -2\Omega(u^* - U^*). \quad (3)$$

Integrating (3) over the flow domain, using the divergence theorem, the vanishing of normal velocity on the upper and lower boundaries, the uniform conditions at large distance and (2), gives

$$2U^*D(V_+ - V_-) = -2\Omega \int [2U^*D - U^*H^*(x^*)] dx^* = -4\Omega U^*A, \quad (4)$$

where $H^*(x^*)$ is the local depth, A is the cross-sectional area of the ridge, and V_- and V_+ are the values of the cross-flow speed far upstream and far downstream. The generation of negative relative vertical vorticity as fluid columns are compressed moving over the ridge thus generates a clockwise change in flow direction determined by the difference

$$V_+ - V_- = -2\Omega A/D, \quad (5)$$

which becomes progressively less important the deeper the flow. Since the flow geometry is independent of y any value of V_- can be enforced by an appropriate choice of the upstream pressure gradient p_x .

Sufficiently far upstream of the ridge the velocity field is uniform horizontally and an Ekman layer solution satisfies the full nonlinear system (1) for arbitrary E and Ro , giving the solution

$$u_0^* + iv_0^* = (U^* + iV_-) \left\{ 1 - \frac{\cosh[(1+i)(2E\delta^2)^{-1/2}(z-\delta)]}{\cosh[(1+i)(2E)^{-1/2}]} \right\}. \quad (6)$$

The nondimensional shear stress on the lower boundary is thus

$$\frac{d}{dz}(u_0 + iv_0)|_{z=0} = (2E\delta^2)^{-1/2}(1+i)(1+iV_-/U^*) \tanh[(1+i)(2E)^{-1/2}], \quad (7)$$

rotated by an angle $\pi/4$ from the outer velocity. For sufficiently small Ekman number the x component of shear stress is negative if V_- exceeds U , which it will for any ridge of nonzero cross-sectional area if the rotation is sufficiently rapid and the interior flow is symmetric about the ridge. The

equations are no longer parabolic in the direction of increasing x . This difficulty is removed here by taking advantage of the y independence of the flow to set $V_- = 0$ far upstream (so $p_x \rightarrow 0$ as $x \rightarrow -\infty$) so the upstream shear stress is always in the x direction. Far downstream, for small Ekman numbers, the x component of wall shear of the ridge is then, from (5),

$$(2E\delta^2)^{-1/2}(U^* + 2\Omega A/D), \quad (8)$$

increasing due to the clockwise rotation of the exterior flow, and outside the Ekman layers, from (5),

$$v \rightarrow -2\Omega A/U^*D, \quad p_x \rightarrow -2\Omega^2 AL/DU^{*2}, \quad \text{as } x \rightarrow \infty. \quad (9)$$

The nondimensional boundary upstream conditions on the flow can thus be written

$$(u, v, w) = (0, 0, 0), \quad \text{on } z = \alpha b(x), \quad (10)$$

$$(u_z, v_z, w) = (0, 0, 0), \quad \text{on } z = \delta, \quad (11)$$

$$(u, v, w) \rightarrow (u_0, v_0, 0)|_{V_- = 0}, \quad \text{as } x \rightarrow -\infty, \quad (12)$$

where the nondimensional parameter, $\alpha = h/L$, gives the average slope of the ridge and $\delta = D/L$ gives the channel aspect ratio. In addition to setting the upstream flow field, rotation also affects the structure of the boundary layer over the ridge and this effect is discussed in greater detail in the following section.

III. BOUNDARY LAYER ANALYSIS, $\text{Re} \gg 1$

We consider system (1) in the limit $\text{Re} \rightarrow \infty$ with Ro fixed. The continuity equation (1d) allows the introduction of a streamfunction ψ defined through

$$u = \psi_z, \quad w = -\psi_x. \quad (13)$$

Then the momentum equations become

$$-\frac{\partial(\psi, u)}{\partial(x, z)} - \text{Ro}^{-1}v = -p_x + \text{Re}^{-1}\nabla^2 u, \quad (14a)$$

$$-\frac{\partial(\psi, v)}{\partial(x, z)} + \text{Ro}^{-1}(u - 1) = \text{Re}^{-1}\nabla^2 v, \quad (14b)$$

$$-\frac{\partial(\psi, w)}{\partial(x, z)} = -p_z + \text{Re}^{-1}\nabla^2 w, \quad (14c)$$

where $\frac{\partial(f, g)}{\partial(x, y)} := f_x g_y - f_y g_x$. Cross differentiation of (14a) and (14c) gives with (14b)

$$-\frac{\partial(\psi, \eta)}{\partial(x, z)} = \text{Ro}^{-1}v_z + \text{Re}^{-1}\nabla^2 \eta, \quad (15a)$$

$$-\frac{\partial(\psi, v)}{\partial(x, z)} = \text{Ro}^{-1}(1 - \psi_z) + \text{Re}^{-1}\nabla^2 v, \quad (15b)$$

where $\eta = u_z - w_x = \psi_{xx} + \psi_{zz} = \nabla^2 \psi$ is the y component of vorticity. The boundary conditions on ψ and v are

$$(\psi, \psi_z, v) = (0, 0, 0), \quad \text{on } z = \alpha b(x), \quad (16)$$

$$(\psi, \psi_{zz}, v) = (\delta, 0, 0), \quad \text{on } z = \delta, \quad (17)$$

$$(\psi, v) \rightarrow \left(\int u_0 dz, v_0 \right), \quad \text{as } x \rightarrow -\infty. \quad (18)$$

A. The outer flow at large Reynolds number

In the limit, $\text{Re} \rightarrow \infty$ with all variables of order unity, (15), (16), (18) reduce to

$$-\frac{\partial(\psi, \eta)}{\partial(x, z)} = \text{Ro}^{-1} \frac{\partial(x, v)}{\partial(x, z)}, \quad (19a)$$

$$-\frac{\partial(\psi, v)}{\partial(x, z)} = \text{Ro}^{-1} \frac{\partial(x, z - \psi)}{\partial(x, z)}, \quad (19b)$$

giving an inviscid outer flow, subject to the inviscid boundary conditions

$$\psi = 0, \quad \text{on } z = \alpha b(x), \quad (20)$$

$$\psi = \delta, \quad \text{on } z = \delta, \quad (21)$$

$$(\psi, v) \rightarrow (z, 0), \quad \text{as } x \rightarrow -\infty. \quad (22)$$

For unidirectional motion (where $\psi_z = u \neq 0$ throughout the flow domain) it is convenient to map the flow domain to a rectangle by taking independent variables (x, ψ) and dependent variables $Z(x, \psi)$. Multiplying Eqs. (19) by the Jacobian $|\partial(x, z)/\partial(x, \psi)| = Z_\psi$ gives

$$-\frac{\partial(\psi, \eta)}{\partial(x, \psi)} = \text{Ro}^{-1} \frac{\partial(x, v)}{\partial(x, \psi)}, \quad (23a)$$

$$-\frac{\partial(\psi, v)}{\partial(x, \psi)} = \text{Ro}^{-1} \frac{\partial(x, z - \psi)}{\partial(x, \psi)}, \quad (23b)$$

i.e.,

$$\eta_x = \text{Ro}^{-1} v_\psi, \quad (24a)$$

$$v_x = \text{Ro}^{-1} Z_\psi - \text{Ro}^{-1}, \quad (24b)$$

which can be combined to give

$$Z_{\psi\psi} - \text{Ro}^2 \eta_{xx} = 0. \quad (25)$$

In (x, ψ) coordinates the Cartesian velocity components become

$$u(x, \psi) = 1/Z_\psi, \quad w(x, \psi) = Z_x/Z_\psi, \quad (26)$$

giving the outer flow velocity component along a streamline as

$$U_{\text{out}}(x, \psi) = (u^2 + w^2)^{1/2} = (1 + Z_x^2)^{1/2} / Z_\psi. \quad (27)$$

Although the system (24) and Eq. (25) appear linear, in (x, ψ) coordinates

$$\eta = \nabla^2 \psi = (1/2) [(1 + Z_x^2)/Z_\psi^2]_\psi - (Z_x/Z_\psi)_x, \quad (28)$$

closing the problem for $Z(x, \psi)$ in (x, ψ) space but rendering the field equation nonlinear. The boundary condition on the ridge becomes simply a condition on the coordinate line $\psi = 0$, giving a problem in a rectangular domain with

$$Z(x, 0) = \alpha b(x), \quad (29a)$$

$$Z(x, \delta) = \delta, \quad (29b)$$

$$Z(x, \psi) \rightarrow \psi, \quad \text{as } |x| \rightarrow \infty. \quad (29c)$$

These equations are equivalent to those derived for stratified, rotating flow by Jacobs [13], although the change in transverse velocity noted here is not discussed there.

B. The inner, boundary layer solution

For Rossby numbers of order unity, the outer solution matches the no-slip condition on the ridge in a viscous layer of thickness $\text{Re}^{-1/2}$ which follows the ridge profile in attached flow. We thus introduce the coordinate $\zeta = \text{Re}^{1/2}\psi$ orthogonal to the surface $\psi = 0$ and the scaled velocity component normal to the surface $W = \text{Re}^{1/2}u_n$ for normal velocity component u_n which vanishes as $\zeta \rightarrow \infty$. Then the boundary layer is governed by the equations

$$UU_\xi + WU_\zeta - \text{Ro}^{-1}V + P_\xi = U_{\zeta\zeta}, \quad (30a)$$

$$UV_\xi + WV_\zeta + \text{Ro}^{-1}(U - 1) = V_{\zeta\zeta}, \quad (30b)$$

$$P_\zeta = 0, \quad (30c)$$

$$U_\xi + W_\zeta = 0. \quad (30d)$$

Here ξ is the arc length along the (curved) lower boundary, $U(\xi, \zeta)$ the (tangential) speed in the ξ direction, $V(\xi, \zeta)$ the speed in the y direction, and $P(\xi, \zeta)$ the pressure. The distances ξ and x are related through the slope, $\alpha b'(x)$, of the ridge; choosing the origins of ξ and x to coincide gives

$$\xi(x) = \int_0^x \sqrt{1 + \alpha^2 b'^2(\bar{x})} d\bar{x}. \quad (31)$$

The boundary conditions on system (30) are

$$[U, V, W] = [0, 0, 0], \quad \text{on } \zeta = 0, \quad (32a)$$

$$[U, V] \rightarrow [U_e(\xi), V_e(\xi)], \quad \text{as } \zeta \rightarrow \infty, \quad (32b)$$

$$[U, V] = [U_0(\zeta), V_0(\zeta)], \quad \text{at } \xi = \xi_0, \quad (32c)$$

$$P \rightarrow P_e(\xi), \quad \text{as } \zeta \rightarrow \infty, \quad (32d)$$

where, from (27), the exterior velocity components are given by $U_e(\xi) = U_{\text{out}}(x, 0)$, $V_e(\xi) = v(x, 0)$, $P_e(\xi) = p(x, 0)$ for $x = x(\xi)$, obtained by inverting (31) and $U_0(\zeta)$, $V_0(\zeta)$ are the usual Ekman layer velocities, valid for arbitrary Re sufficiently far upstream of the ridge, at some $-\xi_0 \gg 1$, so, from (6),

$$U_0(\zeta) + iV_0(\zeta) = 1 - \exp[-(1 + i)(2\text{Ro})^{-1/2}\zeta]. \quad (33)$$

For sufficiently low ridges, system (30) is parabolic and so can be numerically integrated by stepping downstream from the known upstream profile at $\xi = \xi_0$. This integration is described in the Appendix which extends the nonrotating one-dimensional method of [14] to rotating flow with two nonzero horizontal velocity components.

C. The shallow flow limit, $\delta \ll 1$

In general the solution of (25) and (28) can be found only numerically. However, for shallow flows where $\delta \ll 1$, (25) reduces to $Z_{\psi\psi} = 0$ with solution

$$Z(x, \psi) = \alpha b(x)(1 - \psi/\delta) + \psi, \quad (34)$$

giving the depth-independent horizontal velocity components

$$u(x, \psi) = [1 - \Delta b(x)]^{-1}, \quad v(x, \psi) = -(\Delta/\text{Ro}) \int_{-\infty}^x b(x') dx', \quad (35)$$

depending solely on the ridge shape and the fractional height $\Delta = \alpha/\delta$. The velocity along the lower boundary is thus, from (27),

$$U_e(\xi) = u(x, 0)\sqrt{1 + \alpha^2 b'^2} = \sqrt{1 + \alpha^2 b'^2}/[1 - \Delta b(x)], \quad x = x(\xi). \quad (36)$$

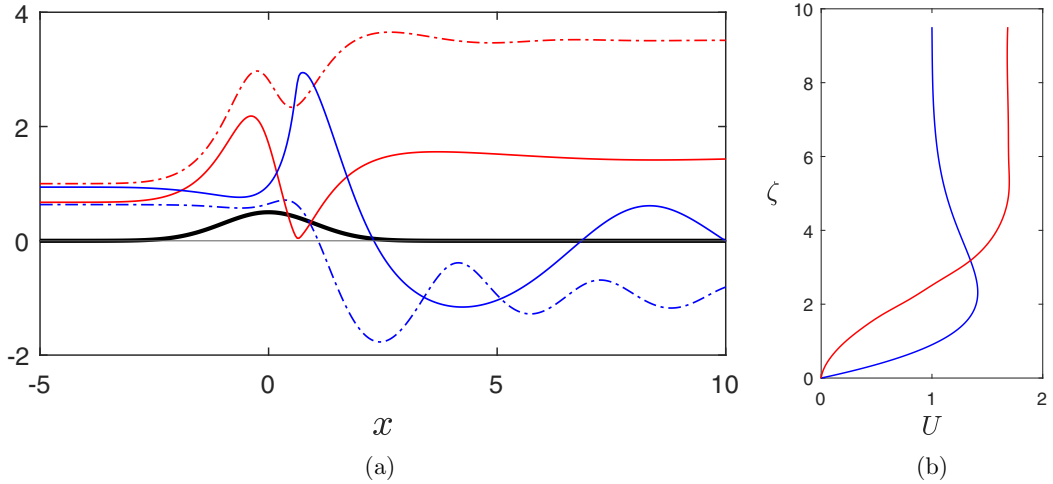


FIG. 2. (a) The nondimensional tangential shear stress (red) at the lower boundary in the direction orthogonal to the ridge, $\tau_1(x) = \hat{\xi} \cdot \boldsymbol{\tau}(x)$, and the nondimensional boundary-layer displacement thickness (blue), $d(x)$, as functions of position x for a Gaussian ridge of maximum fractional depth $\Delta = 0.5$ for Rossby numbers $Ro = 0.5$ (dashed-dotted) and $Ro = 1.1$ (solid lines). The ridge profile is shown in black. A decaying inertial oscillation is visible in the displacement thickness for both values of Ro . (b) The corresponding profiles of the nondimensional tangential component of velocity, $U(\xi(x), \zeta)$, as a function of the scaled normal coordinate, ζ , for $Ro = 1.1$. The red curve gives the profile at $x = 0.63$ corresponding to the minimum in the wall shear and the blue curve gives the profile at $x = 4.23$ corresponding to the minimum in the displacement thickness.

The shallow flow solution (35) provides precisely the outer flow required for the numerical solution of the boundary layer equations (30) as formulated in the Appendix. Two quantities are of particular interest: the scaled boundary-layer displacement thickness,

$$d(x) = \int_0^\infty [1 - U(\xi(x), \zeta)/U_e(\xi(x))] d\zeta, \quad (37)$$

and the shear stress at the bottom boundary,

$$\boldsymbol{\tau}(x) = U_\zeta(\xi(x), 0)\hat{\xi} + V_\zeta(\xi(x), 0)\hat{y}, \quad (38)$$

for unit vectors $\hat{\xi}$ and \hat{y} in the corresponding coordinate directions. Figure 2(a) shows the first component of the stress, $\tau_1(x) = \hat{\xi} \cdot \boldsymbol{\tau}(x)$, and displacement $d(x)$ for a Gaussian ridge $b(x) = \exp(-x^2/2)$ of fractional height $\Delta = 0.5$. Negative $\tau_1(x)$ corresponds to recirculation in the planes $y = \text{constant}$. When the rotation is reasonably strong ($Ro = 0.5$) the flow direction rotates, from (9), by $\tan^{-1}[(\Delta/Ro) \int b(x) dx] = \tan^{-1} \sqrt{2/\pi}$ clockwise on passing over the ridge and the component of the velocity in the x direction increases, as does the shear stress at the wall as in (8). The adverse pressure gradient in the lee of the ridge causes a small local decrease in wall stress. The rotation of the external velocity also leads to an internal maximum of the downstream velocity which exceeds the free-stream velocity [as in Fig. 2(b) for $Ro = 1.1$]. The inflow to the boundary layer increases the volume flux in the layer compared with that in the free stream and leads to a negative displacement thickness downstream from the ridge. The adjustment to the new displacement thickness is through a viscously damped inertial oscillation, where fluid particles oscillate about their equilibrium level with frequency 2Ω and wavelength determined by a balance between the advection and Coriolis terms in (30a), (30b) and so of order Ro , as can be seen by comparing with the displacement thickness for $Ro = 1.1$ where the wavelength is approximately 2.2 times longer. For $Ro = 1.1$ nonlinear advection is more important making the adverse pressure gradient in the lee of the ridge

larger and causing the wall shear stress to fall to a minimum of approximately 0.04. For larger Ro the wall shear stress becomes negative corresponding to a region of reversed flow near the wall (as in Fig. 5 below). The boundary layer equations are no longer downstream parabolic and stepping from upstream conditions fails. This difficulty is traditionally [14] overcome by setting all negative velocities to zero to keep the system downstream parabolic. This *ad hoc* modification works remarkably well as velocities in the separation bubble tend to be small. The difficulty does not arise in the finite-element method of Sec. IV below as it has no requirement that the system be downstream parabolic. The thickening of the boundary layer near the point of minimum wall shear, even for unidirectional flow, is visible in the rapid increase of the displacement thickness there. Figure 2(b) shows profiles of U as a function of the scaled normal coordinate, ζ , for the $Ro = 1.1$ solution of Fig. 2(a). The red curve gives the profile at $x = 0.63$ corresponding to the minimum in the wall shear and so is almost vertical at the wall. The blue curve gives the profile at $x = 4.23$ corresponding to the minimum in the displacement thickness, showing the jetlike flow in the interior of the layer which increases the mass flux above the corresponding mean flow flux, thinning the layer and giving the negative displacement thickness.

IV. NUMERICAL SIMULATION OF THE FULL EQUATIONS FOR SHALLOW FLOW

We present here numerical simulations of the full nonlinear system (1) at high Re and small channel aspect ratio δ , comparing them to the boundary layer integrations in Sec. III which correspond to the solutions here in the limit $Re \rightarrow \infty$, $\delta \rightarrow 0$. For the shallow flow computations of this section only, we introduce the vertical scaling $\hat{z} = z^*/D = z/\delta$ so that the geometry is fixed independently of δ . The lower boundary is then taken as the Gaussian ridge occupying half the fluid depth, $\hat{z} = \Delta \exp(-x^2/2)$, with $\Delta = 0.5$, as in Fig. 2. We truncate the computational domain at $x = \pm 10$ and define

$$\Omega^s := \{(x, z) \in \mathbb{R}^2, -10 < x < 10, b(x) < \hat{z} < 1\}.$$

We introduce a subtessellation \mathcal{T}_h of Ω^s into triangles $T \in \mathcal{T}_h$ and use the following finiteelement spaces of continuous piecewise linear finite elements on \mathcal{T}_h :

$$\begin{aligned} \mathcal{V}_h &:= \{v \in C(\bar{\Omega}^s)^3, v_i|_T \in P_1(T) \ \forall T \in \mathcal{T}_h, v_i = 0 \text{ on } \Gamma_i^d, i = 1, 2, 3\}, \\ \mathcal{L}_h &:= \{p \in C(\bar{\Omega}^s), p|_T \in P_1(T) \ \forall T \in \mathcal{T}_h\}. \end{aligned}$$

The Dirichlet part of the boundary Γ_i^d differs slightly between the components. For $i = 1, 2$ it is given by the lower boundary, where no-slip conditions (10) are imposed and the left (upstream) boundary, where the inflow profile (33) is imposed for $U = 1$. Γ_3^d includes additionally the upper (symmetry) boundary, where the symmetry condition (11) is imposed. No constraint is applied to the variational formulation at the downstream boundary and thus it satisfies the natural boundary condition there (see, e.g., [15]) giving the outflow conditions,

$$Re^{-1}u_x - p = 0, \quad v_x = 0, \quad w_x = 0.$$

For brevity we write $U := (u, v, w)$, $\bar{U} := (u, w)$, $\bar{\nabla} := (\partial_x, \partial_z)$, and $\bar{\nabla}_\delta := (\partial_x, \delta^{-1}\partial_z)$. By $U^d = (u^d, v^d, w^d)$ we denote an extension of the Dirichlet data to Ω^s , i.e., the inflow profile (6) for u and v on the upstream boundary and the zero function for w on the remaining Dirichlet parts.

The discrete variational formulation corresponding to (1a)–(1c) reads: Find $U \in U^d + \mathcal{V}_h$, $p \in \mathcal{L}_h$, such that

$$\begin{aligned} &(\bar{U} \cdot \bar{\nabla} U, \phi)_{\Omega^s} + Re^{-1}(\bar{\nabla}_\delta U, \bar{\nabla}_\delta \phi)_{\Omega^s} - Ro^{-1}(v, \phi_1)_{\Omega^s} \\ &+ Ro^{-1}(u - 1, \phi_2)_{\Omega^s} - (p, \bar{\nabla} \cdot \phi)_{\Omega^s} + (\bar{\nabla} \cdot \bar{U}, \eta)_{\Omega^s} \\ &+ s_u(U, \phi) + s_p(p, \eta) = 0 \quad \forall \phi \in \mathcal{V}_h, \eta \in \mathcal{L}_h. \end{aligned} \tag{39}$$

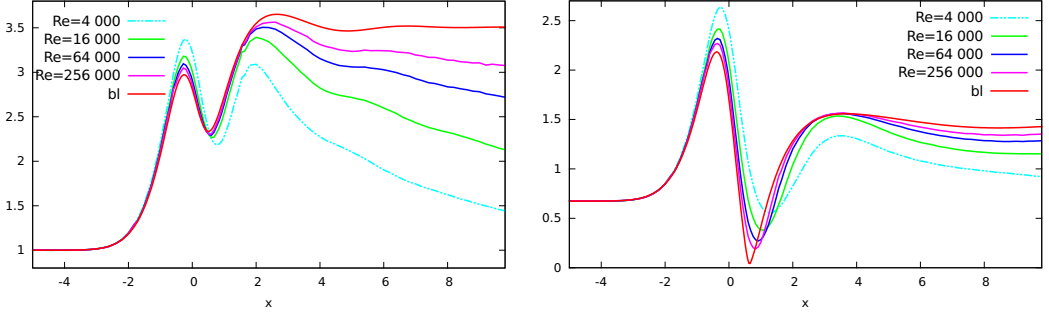


FIG. 3. The wall shear stress for $\delta = 0.1$ and $\text{Ro} = 0.5$ (left) and $\text{Ro} = 1.1$ (right) for different Re , compared to the boundary layer calculations for $\delta \rightarrow 0$, $\text{Re} \rightarrow \infty$.

Due the lack of inf-sup-stability of the discrete spaces and to handle convection-dominated regimes for high Re , we add the weakly consistent Continuous Interior Penalty stabilization terms defined by

$$s_u(U, \phi) = \gamma_u \sum_{e \in \mathcal{E}_h} |e|^2 (\llbracket \nabla U \rrbracket, \llbracket \nabla \phi \rrbracket)_e,$$

$$s_p(p, \eta) = \gamma_p \sum_{e \in \mathcal{E}_h} \max \left\{ |e|^3 \frac{\delta}{\nu}, \frac{|e|^2}{\|\bar{U}\|} \right\} (\llbracket \bar{\nabla} p \rrbracket, \llbracket \bar{\nabla} \eta \rrbracket)_e,$$

where $\llbracket \cdot \rrbracket$ denotes the jump operator over interior edges $e \in \mathcal{E}_h$ and γ_u, γ_p are positive parameters [8].

All the simulation results have been obtained with the finite-element library FreeFem++ [16]. For the visualization, we use the visualization tool ParaView [17]. We use a triangulation with 192 682 vertices (379 024 triangles), which is highly refined along the lower boundary, in order to resolve the boundary layer for high Re . To solve the nonlinear system of equations, we use a fixed-point iteration based on the Oseen linearization of the Navier-Stokes equations: For $l = 1, \dots$, find $U^l \in U^d + \mathcal{V}_h$, $p^l \in \mathcal{L}_h$, such that

$$\begin{aligned} & (\bar{\beta}^l \cdot \bar{\nabla} U^l, \phi)_{\Omega^s} + \text{Re}^{-1} (\bar{\nabla}_\delta U^l, \bar{\nabla}_\delta \phi)_{\Omega^s} - \text{Ro}^{-1} (v^l, \phi_1)_{\Omega^s} \\ & + \text{Ro}^{-1} (u^l - 1, \phi_2)_{\Omega^s} - (p^l, \bar{\nabla} \cdot \phi)_{\Omega^s} + (\bar{\nabla} \cdot \bar{U}^l, \eta)_{\Omega^s} \\ & + s_u(U^l, \phi) + s_p(p^l, \eta) = 0 \quad \forall \phi \in \mathcal{V}_h, \eta \in \mathcal{L}_h, \end{aligned}$$

where $\beta^l := \frac{1}{2}(U^{l-1} + U^{l-2})$ for $l \geq 2$ and $\beta_1 = U^0$ for a suitable starting value U^0 . Although its rate of convergence is in general worse compared to a standard Newton iteration, we expect this fixed-point iteration to be more robust, and for this reason better suitable to give an indication on the existence or nonexistence of stationary solutions.

A. The attached boundary layer regime, $\text{Ro} < 1.2$

Figure 3 compares the nondimensional wall shear stress,

$$\tau = \partial_n u / (E^{1/2} \delta),$$

for $\delta = 0.1$ and $\text{Ro} \in \{0.5, 1.1\}$ at increasing Reynolds numbers $\text{Re} = 4000, 16000, 64000$, and 256000 with the boundary layer solutions of Fig. 2, corresponding to the limit $\delta \rightarrow 0$, $\text{Re} \rightarrow \infty$. We observe convergence for $\text{Re} \rightarrow \infty$, although high Reynolds numbers are needed to get close to the results obtained from the boundary layer computations. Notice that we do not expect to fully reach the latter curve, as δ is fixed to 0.1. The solution stays attached to the

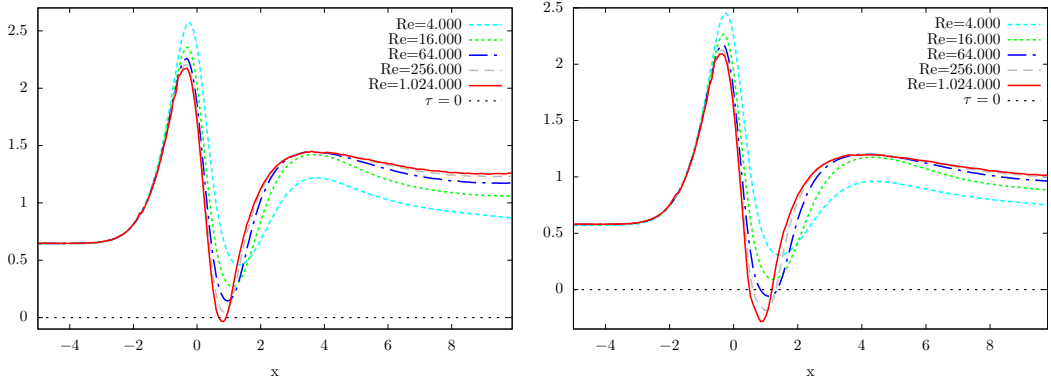


FIG. 4. The wall shear stress for $\delta = 0.1$ and $Ro = 1.2$ (left) and $Ro = 1.5$ (right) for various Re .

boundary for all tested Reynolds numbers, i.e., up to $Re = 256\,000$. The finite-element method appears to give reasonable results up to very large Reynolds numbers.

B. Separated, steady, recirculating flow, $Ro \geq 1.2$

For $Ro \geq 1.2$, the flow detaches in the lee of the ridge (for $\delta \rightarrow 0$, $Re \rightarrow \infty$). The boundary layer equations (30a) and (30b) are no longer downstream parabolic and so, as noted in Sec. III, cannot be used to compute an inner solution by stepping downstream. The finite-element formulation solves full system (1) and so has no such restrictions. Figure 4 shows numerical results for fixed $\delta = 0.1$ and $Ro = 1.2$ and $Ro = 1.5$, at various values of Re . For $Ro = 1.2$ the boundary layer detaches at $Re = 1.024 \times 10^6$, i.e., the wall shear stress takes negative values in the lee of the ridge, at $x \approx 0.8$. For $Ro = 1.5$, this happens earlier, by $Re \geq 64\,000$. For both Rossby numbers, the method gives stationary states up to (at least) $Re = 1.024 \times 10^6$.

Figure 5 (top) shows isolines in the x - z plane of the streamfunction for $Re = 256\,000$ and $Ro = 1.2$, $Ro = 1.5$, and $Ro = 2$. Since the y component of velocity is nonzero these are vertical

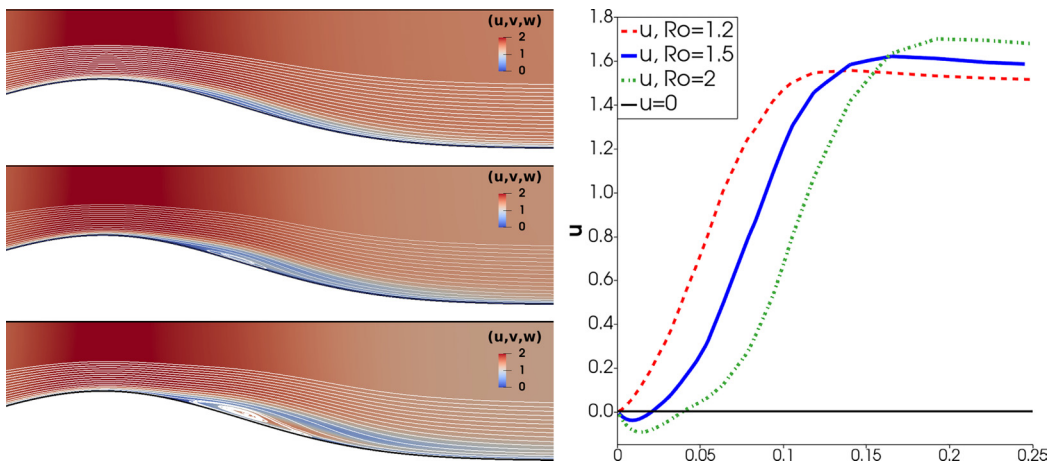


FIG. 5. Left: Streamlines in the lee of the ridge at $Re = 256\,000$ for $Ro = 1.2$, 1.5 , and 2 . Note that the picture shows only a part of the simulation domain. The flow detaches for $Ro = 1.5$ and $Ro = 2$ at $x \approx 0.75$ and $x \approx 0.6$, respectively. Right: Profiles normal to the lower boundary through the center of the eddy of the horizontal velocity u for these cases.

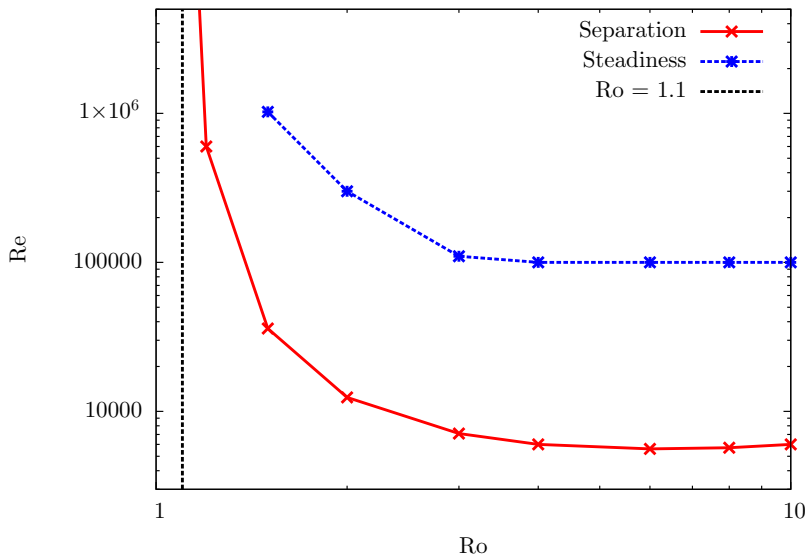


FIG. 6. Shallow flow, $\delta = 0.1$. Red solid curve: The smallest value of Re , at fixed Ro , for which the flow separates. For all pairs (Ro, Re) above the line a separation bubble occurs in the lee of the ridge. Blue dotted curve: The largest value of Re , at fixed Ro , for which a stationary solution was obtained by the fixed-point algorithm. The vertical dashed line shows the upper bound at $Ro = 1.1$ for attached flow in the boundary layer analysis of Sec. III.

sections of stream surfaces, referred to subsequently, for brevity, as streamlines. While for $Ro = 1.2$ the flow is still attached to the boundary, the flow detaches for $Ro = 1.5$ and $Ro = 2$ and a separation bubble becomes clearly visible. Figure 5 (bottom) shows vertical profiles through the eddy of the horizontal velocity u . The negative values show the reverse flow for $Ro = 1.5$ and $Ro = 2$.

Figure 6 shows the critical Reynolds numbers (red solid curve) for boundary layer separation as a function of Rossby number. Separation occurs at all points above the curve while at points below the curve the flow remains attached. For the ridge geometry here, the flow remains attached for Reynolds numbers, $Re \leq 5600$, at all rotation rates, with separation depending solely on the Reynolds number for $Ro \geq 6$. At smaller Rossby numbers, $Ro < 1.2$, when rotational effects become significant, the flow remained attached to the boundary for all tested configurations, i.e., up to at least $Re = 1.024 \times 10^6$. With decreasing Ro the curve approaches the vertical dashed line showing the upper bound at $Ro = 1.1$ for attached flow in the boundary layer analysis of Sec. III. At any fixed $Ro > 1.1$ there exists a critical Reynolds number, higher than the Reynolds number for separation, above which the fixed-point algorithm is unable to find a stationary solution. This gives an indication that above some value of Re no stable stationary solution exists. The values for the disappearance of stationary solutions are shown by the blue dotted curve in Fig. 6 which shows the same qualitative behavior as the separation Reynolds number curve. For Rossby numbers greater than 1.2 there is thus a considerable range of Reynolds numbers where a steady recirculating separation bubble is present in the lee of the ridge.

V. DEEP FLOW OVER A RIDGE

Lighthill [18] shows that in a frame moving with the upstream speed U^* the ridge can be regarded as traveling steady forcing effect which in deep flow generates small disturbances governed by the inertial wave equation and so satisfying

$$k^2(k^2 + m^2) = m^2/Ro^2, \quad (40)$$

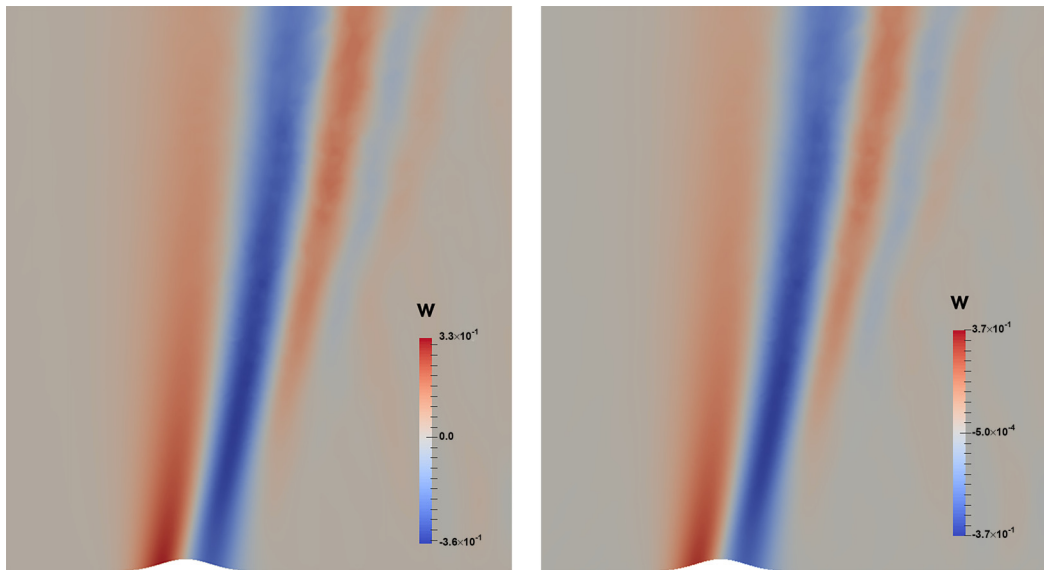


FIG. 7. The vertical velocity component w for deep flow with $Ro = 0.1$ at $Re = 400$ (left) and $Re = 10\,000$ (right). The flow field is almost unaltered when the Reynolds changes by a factor of 25. The mesh is highly refined around the ridge and the figure shows approximately half the simulation domain.

where (k, m) are the nondimensional (x, z) wavenumbers normalized on $1/L$. Lighthill illustrates in Fig. 11 of [18] that (40) implies a horizontal wavenumber cutoff k_c such that

$$|k| < k_c = 1/Ro, \quad (41)$$

with $|k|$ asymptoting to k_c with increasing m . In the shallow flow of Sec. III C the vertical wave length is necessarily small, of the order of the fluid depth, so $m \gg 1$ and $|k| \rightarrow k_c$. These are the boundary-layer inertial oscillations, of frequency 2Ω , noted in Sec. III C, of exponentially small amplitude in the interior of the flow where the flow is given by (34). In deeper flows progressively more vertical modes contribute [4] until the vertical behavior can be treated as a continuum of modes [3,4]. To admit this inertial wave field and thus assess the effect of the absence of an upper rigid boundary, we revert to the variable $z = z^*/L$, truncating the computational domain at $z = 100$ and impose the boundary conditions $(u, v, w) = (1, 0, 0)$ at the left inflow boundary and on the top boundary. This is equivalent to setting $\delta = 100$ in the variational formulation of (39) once the space \mathcal{V}_h has been modified to accommodate Dirichlet boundary conditions on the upper boundary for all variables. To give a ridge of aspect ratio of order unity, as in the experiments of [3], the ridge profile is taken as $z = \alpha \exp(-x^2/2)$, with $\alpha = 1/2$. This gives bounded ridge slopes that are ten times those of Sec. IV and is reflected below in separation at much smaller values of the Reynolds number. The effect of the infinite slope of the cylinder is considered in Sec. VI.

Figure 7 shows the vertical velocity component w for $Ro = 0.1$ at $Re = 400$ and $10\,000$. The flow patterns are very similar. This accords with the analysis in [3,4] showing that the leading order viscous effect in deep flow at small Rossby number is the introduction of a downstream decay of the lee wave wake with a scale of order Re^{-1} and a downstream displacement of the phase lines at large Re of order $(Ro Re)^{-1}$.

Figure 8, as for Fig. 6, shows at fixed Rossby number the largest values of Reynolds number at which the flow remained attached (red curve) and at which the fixed-point iteration converged (blue curve). The qualitative behavior of the curves is very similar but the critical Reynolds numbers are an order of magnitude smaller in the deep flow. As noted above, this is a consequence of the ridge slope's being an order of magnitude larger here. At fixed Rossby number, greater than 1.5,

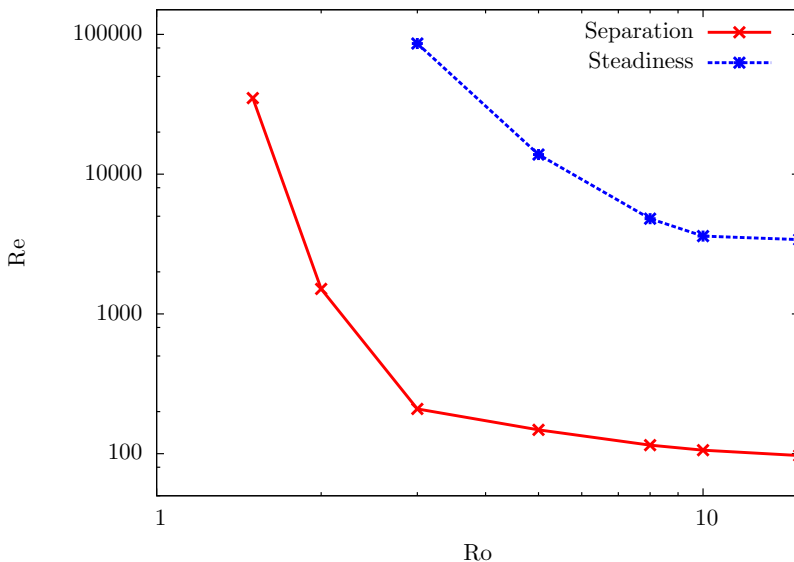


FIG. 8. Deep flow, $\delta = 100$. Red solid curve: The smallest value of Re , at fixed Ro , for which the flow separates. Blue dotted curve: The largest value of Re , at fixed Ro , for which a stationary solution was obtained by the fixed-point algorithm.

there again exists a considerable range of Reynolds numbers where a steady recirculating separation bubble is present in the lee of the ridge.

Figure 9 shows the vertical velocity w and streamlines in the lee of the ridge for deep flow and weak rotation with $Ro = 3$ at $Re = 200, 1000$. The flow is attached for $Re = 200$ but has separated by $Re = 1000$ with a steady recirculating separation bubble visible.

VI. FLOW OVER A HORIZONTAL CYLINDER

To capture more closely the geometry of the experiments reported in [3], this section considers flow over a horizontal right circular cylinder. The variational formulation is again given by (39) with $\delta = 1$. We use an ellipsoidal simulation domain with semiaxes of size 60 (vertically) and 150 (horizontally) from which a circle of radius 0.5 (representing an infinitely long cylinder in transversal direction), is extracted. We set $U^d = (1, 0, 0)$ on the outer boundary of the ellipsoid and $U^d = (0, 0, 0)$ on the cylinder.

Figure 10 shows a pair of streamlines for each of (a), (b) $Ro = 0.5$ and (c), (d) $Ro = 2$ at Reynolds numbers Re chosen so the flow is attached to the cylinder at the lower Re (a), (c) and detached at the higher (b), (d). The lower Ro flow remains attached at significantly higher Re but in

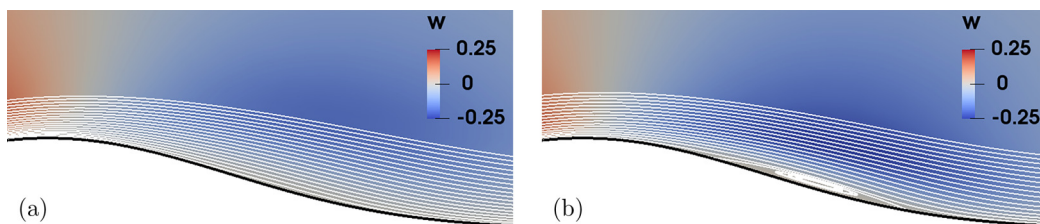


FIG. 9. The vertical velocity w and streamlines in the lee of the ridge for deep flow and weak rotation, $Ro = 3$. (a) $Re = 200$, attached flow. (b) $Re = 1000$, separated flow with a stable separation bubble.

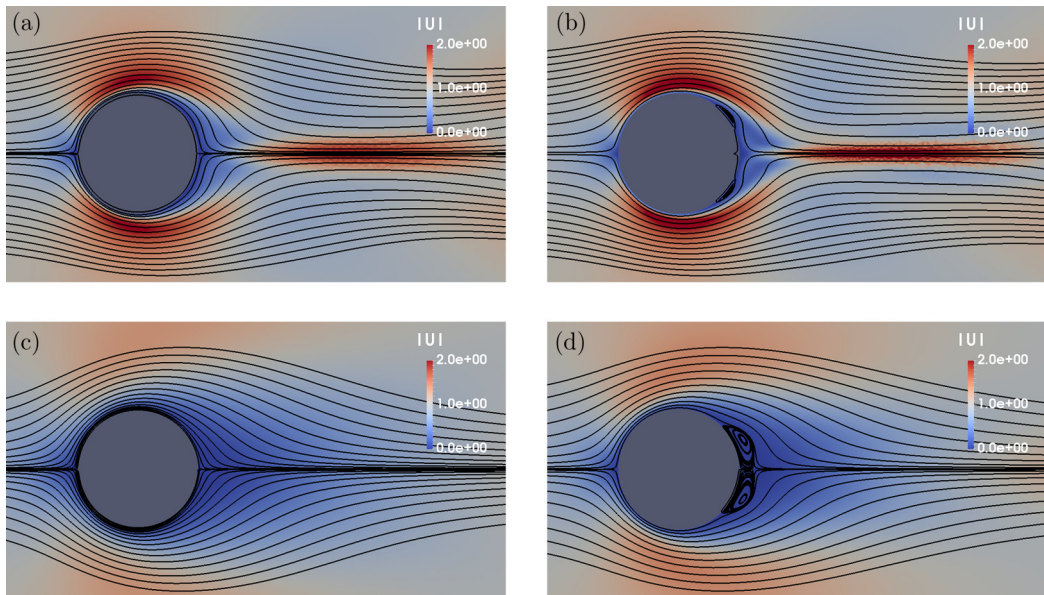


FIG. 10. Streamlines for $(\text{Ro}, \text{Re}) =$ (a) $(0.5, 200)$, (b) $(0.5, 600)$, (c) $(2, 15)$, and (d) $(2, 50)$. The coloring shows the magnitude of the velocity (u, w) . The figure shows only a small part of the simulation domain.

both cases the steep obstacle gradient at the rear of the cylinder, and the concomitant strong adverse pressure gradient, induces separation at far lower Reynolds numbers than in flow over the smooth ridge. The inertial wave alternatively compresses and accelerates and then expands and decelerates a jetlike flow along the axis in the lee of the cylinder. Figure 11 shows vertical profiles through the jet of the horizontal velocity u at downstream stations $x = 1, 2, 3,$ and 4 for the flow in Fig. 10(b). The jet is narrow with almost twice the free-stream speed at $x = 2$ but wide with a velocity deficit giving a speed of two-thirds the free-stream speed at $x = 4$.

As in Figs. 6 and 8, Fig. 12 shows for fixed Rossby number the lowest Re for which separation occurs and the highest Re for which the fixed-point iteration converged. The curves behave qualitatively very similarly to those of Figs. 6 and 8: as $\text{Ro} \rightarrow 0$ is the critical Reynolds number for convergence, Re_{crit} increases rapidly, showing the existence of steady solutions at high Re , and for weakly rotating flow, $\text{Ro} \rightarrow \infty$, Re_{crit} asymptotes to the constant value ($\text{Re}_{\text{crit}} \approx 160$ here) of nonrotating flow. For Reynolds numbers of order 200 and larger the range of values of Rossby numbers for which steady separated solutions exist is small and becomes smaller with increasing Reynolds number, almost vanishing by $\text{Re} = 1000$. These Reynolds numbers include the parameter regime investigated in [3] and supports their observation that separation and unsteadiness appear simultaneously. Figure 13 shows the Re_{crit} curve over a smaller range of Reynolds numbers with the superposed experimental observations of [3] (Fig. 7) that are closest to the transition between steady and unsteady solutions. The qualitative form of the numerical curve appears to capture the experimentally observed separation between steady and unsteady flow. Two experimental points for unsteady flow lie just below the numerical curve. The deviation is within the range of experimental fluctuations and numerical error. In the numerical solution, numerical diffusion could lead to convergence to stationary states on the discrete level that are not stationary states on the continuous level so the critical curve in the continuous limit would lie slightly below the plotted curve. In the experiments even small disturbances to the flow might be of sufficient magnitude to trigger instability below the theoretical threshold. Even with this deviation the numerical curve seems to capture the experimental results well over the whole range. There appears to be a break in the slope of the curves for both the numerical and experimental results at a Rossby number of order unity.

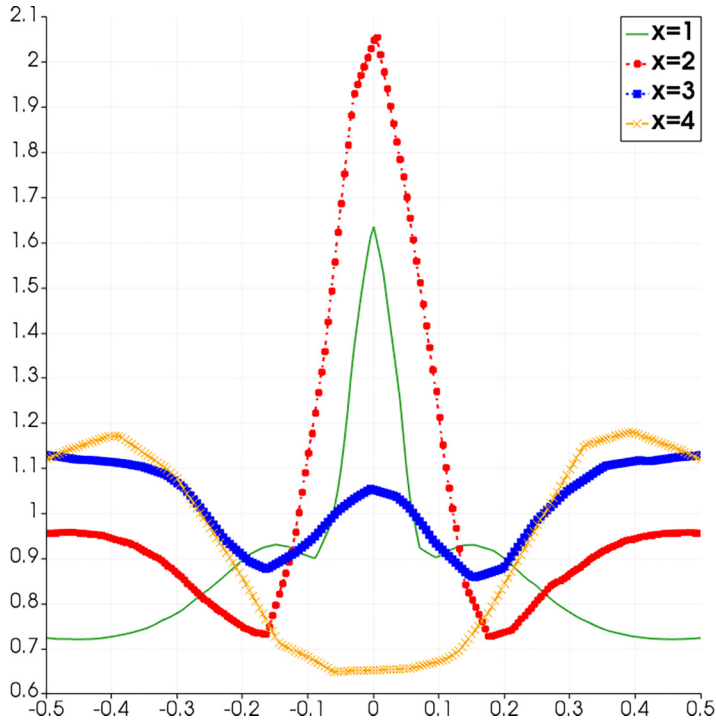
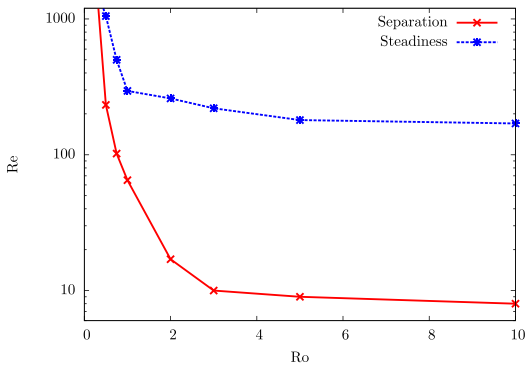


FIG. 11. Vertical profiles through the lee jet of the horizontal velocity u at downstream stations $x = 1, 2, 3,$ and 4 for the flow in Fig. 10(b) where $Ro = 0.5$ and $Re = 600$.

This appears to be related to the horizontal wavenumber cutoff k_c of (41). The cylinder has scaled length of order unity, thus predominantly generating disturbances with horizontal wavenumbers of order unity. Once the Rossby number exceeds unity, $k_c < 1$ and the range of energetic wavenumbers



Ro	0.3	0.5	0.75	1	2	3	5	10
Re_{crit}	1640	1050	500	295	260	220	180	170
$Ro \cdot Re_{crit}$	492	525	375	295	520	660	900	1700

FIG. 12. Left: As Fig. 8, but for deep flow over a cylinder. Red solid curve: The smallest value of Re , at fixed Ro , for which the flow separates. Blue dotted curve: The largest value of Re , at fixed Ro , for which a stationary solution was obtained by the fixed-point algorithm. Right: The largest Reynolds number Re_{crit} , for which a stationary solution was obtained by the fixed-point algorithm for fixed Ro and product $RoRe_{crit}$.

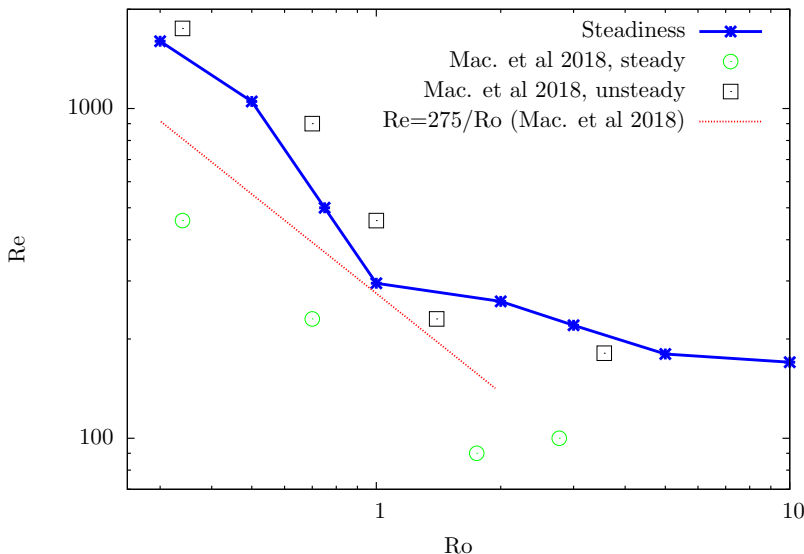


FIG. 13. Comparison of the critical Reynolds numbers found by numerical simulations (blue curve) against the experimental results in [3]. Green circles indicate combinations of Ro and Re , for which steady solutions were observed experimentally; black squares indicate unsteady solutions.

contributing to the wavefield decreases significantly as the flow transitions to one where inertial effects are less important.

Based on their analysis of the lee-wave wake at large Reynolds number [3] postulate that the division between steady and unsteady flow is of the form $RoRe_{crit} = C$ with the experimental results giving $C = 275$. This curve is included in Fig. 13 and captures the division in the flow regime there well. The table in Fig. 12 shows that the relation may not capture the division so well in other flow regimes.

VII. CONCLUSION

Motivated by the geophysical relevance of rotating flow over topography in the atmosphere [1] and ocean and by recent theoretical results and laboratory experiments [3] we have discussed steady attached flow, boundary layer separation, transition to unsteady flow, and flow patterns in the three numerical examples of shallow and deep flow over a Gaussian ridge and deep flow over a horizontal cylinder using a stabilized equal-order finite-element method with Continuous Interior Penalty stabilization. This technique has the advantage of obtaining steady solutions at high Reynolds numbers. For shallow flow (with aspect ratio $\delta = D/L \rightarrow 0$) the solutions were compared with integration of the boundary layer equations valid in the limit $Re \rightarrow \infty$. The finite-element results for $\delta = 0.1$ approached the boundary layer results with increasing Reynolds number and in the region of attached flow the finite-element results converged for Reynolds numbers of order 10^6 . In deep flow over the ridge the inertial wave wake discussed in [3,4] appeared. The computations for deep flow over a cylinder included the parameter regime of the experiments of Machicoane *et al.* [3] and reproduced many of the features observed there.

In all three cases the flow was steady and attached for sufficiently small Reynolds number and also at all Rossby numbers below a critical value of order unity. As the Reynolds number was increased at fixed Rossby number above the critical Rossby number for attachment, the flow separated in the lee of the ridge and a steady separation bubble appeared. At higher Reynolds numbers the fixed-point iteration failed to converge. In flow over a cylinder this coincided closely

with the appearance of unsteady flow in the experiments of [3]. The Reynolds numbers above which separation and, subsequently, unsteadiness appear decrease by an order of magnitude in moving from shallow to deep flow, as the ridge slope increases by a factor of 10, and by another order of magnitude in moving from the smooth ridge to the cylinder, with its infinite slope at the rear stagnation point. In all cases it appears that sufficiently strong rotation allows the flow to remain attached at arbitrarily large Reynolds numbers.

ACKNOWLEDGMENT

We are grateful to the referees for helpful comments and suggestions on presentation.

APPENDIX: THE BOUNDARY LAYER INTEGRATION

The method here extends the nonrotating one-dimensional method of [14] to rotating flow with two nonzero horizontal velocity components. The method is also modified to allow a spectral solution using an expansion in Laguerre polynomials. In (30) we write $(U, V) = (U_e + \tilde{u}, V_e + \tilde{v})$ so $(\tilde{u}, \tilde{v}) \rightarrow 0$ as $\zeta \rightarrow \infty$. Then the ξ -momentum equation (30a) becomes

$$U\tilde{u}_\xi + W\tilde{u}_\zeta = \tilde{u}_{\zeta\zeta} + a\tilde{v} - U_{e\xi}\tilde{u}, \quad (\text{A1})$$

where $a = \text{Ro}^{-1}$ and the far-field pressure satisfies

$$P_{e\xi} = -U_e U_{e\xi} + aV_e. \quad (\text{A2})$$

Substituting (A1) into the continuity equation and rearranging gives

$$(W/U)_\zeta = -(U_e U_{e\xi} + a\tilde{v} + \tilde{u}_{\zeta\zeta})/U^2. \quad (\text{A3})$$

On the solid boundary, $\zeta = 0$, $U = 0$ for all ξ , so $U_\xi = 0$ and hence $W_\zeta = 0$. Thus,

$$\lim_{\zeta \rightarrow 0} (W/U) = \lim_{\zeta \rightarrow 0} (W_\zeta/U_\zeta) = 0, \quad (\text{A4})$$

and (A3) can be integrated from zero on the wall to give W/U at fixed ξ . The momentum equations (30a) and (30b) then become

$$\tilde{u}_\xi = -(W/U)\tilde{u}_\zeta + (\tilde{u}_{\zeta\zeta} + a\tilde{v} - U_{e\xi}\tilde{u})/U, \quad (\text{A5a})$$

$$\tilde{v}_\xi = -(W/U)\tilde{v}_\zeta + (\tilde{v}_{\zeta\zeta} - a\tilde{u} - V_{e\xi}\tilde{u})/U. \quad (\text{A5b})$$

It is convenient to obtain the outer flow and to discuss the solutions in the unstretched coordinate x . Multiplying (A5) by $\xi_x = \sqrt{1 + \alpha^2 b^2(x)}$ gives

$$\tilde{u}_x = -\xi_x [(W/U)\tilde{u}_\zeta + (\tilde{u}_{\zeta\zeta} + a\tilde{v})/U] - U_{ex}\tilde{u}/U, \quad (\text{A6a})$$

$$\tilde{v}_x = -\xi_x [(W/U)\tilde{v}_\zeta + (\tilde{v}_{\zeta\zeta} - a\tilde{u})/U] - V_{ex}\tilde{u}/U. \quad (\text{A6b})$$

Equations (A6) and (A3) are solved spectrally in ζ by expressing \tilde{u} and \tilde{v} as the product of a decaying exponential and a series of Laguerre polynomials through their values at the Laguerre interpolation points, expressing (A3) as a first-order differential equation using a differentiation matrix, inverting to obtain W/U at the interpolation points, and advancing in x using (A6) and a stiff ordinary differential equation solver.

-
- [1] P. J. Mason and R. I. Sykes, Separation effects in Ekman layer flow over ridges, *Q. J. Roy. Meteorol. Soc.* **105**, 129 (1979).
 [2] K. J. Richards, D. A. Smeed, E. J. Hopfinger, and G. C. D'Hières, Boundary-layer separation of rotating flows past surface-mounted obstacles, *J. Fluid Mech.* **237**, 343 (1992).

- [3] N. Machicoane, V. Labarre, B. Voisin, F. Moisy, and P-P. Cortet, Wake of inertial waves of a horizontal cylinder in horizontal translation, *Phys. Rev. Fluids* **3**, 034801 (2018).
- [4] E. Johnson, The effects of obstacle shape and viscosity in deep rotating flow over finite-height topography, *J. Fluid Mech.* **120**, 359 (1982).
- [5] C. H. Williamson, Vortex dynamics in the cylinder wake, *Annu. Rev. Fluid Mech.* **28**, 477 (1996).
- [6] J. Douglas and T. Dupont, Interior penalty procedures for elliptic and parabolic Galerkin methods, in *Computing Methods in Applied Sciences*, edited by R. Glowinski and J. L. Lions (Springer Berlin Heidelberg, Berlin, Heidelberg, 1976), pp. 207–216.
- [7] E. Burman and P. Hansbo, Edge stabilization for the generalized Stokes problem: A continuous interior penalty method, *Comput. Methods Appl. Mech. Eng.* **195**, 2393 (2006).
- [8] E. Burman, M. Fernández, and P. Hansbo, Continuous interior penalty finite element method for Oseen’s equations, *SIAM J. Numer. Anal.* **44**, 1248 (2006).
- [9] G. G. Tong, D. Kamensky, and J. A. Evans, Skeleton-stabilized divergence-conforming B-spline discretizations for incompressible flow problems of high Reynolds number, *Comput. Fluids* **248**, 105667 (2022).
- [10] R. C. Moura, A. Cassinelli, A. F. da Silva, E. Burman, and S. J. Sherwin, Gradient jump penalty stabilisation of spectral/*hp* element discretisation for under-resolved turbulence simulations, *Comput. Methods Appl. Mech. Eng.* **388**, 114200 (2022).
- [11] M. A. Fernández, Incremental displacement-correction schemes for incompressible fluid-structure interaction: Stability and convergence analysis, *Numer. Math.* **123**, 21 (2013).
- [12] E. Burman, M. A. Fernández, and S. Frei, A Nitsche-based formulation for fluid-structure interactions with contact, *ESAIM: Math. Modell. Numer. Anal.* **54**, 531 (2020).
- [13] S. Jacobs, On stratified flows over bottom topography, *J. Mar. Res.* **22**, 223 (1964).
- [14] L. Prandtl, Zur Berechnung der Grenzschichten, *Z. Angew. Math. Mech.* **18**, 77 (1938).
- [15] J. Heywood, R. Rannacher, and S. Turek, Artificial boundaries and flux and pressure conditions for the incompressible Navier-Stokes equations, *Int. J. Numer. Methods Fluids* **22**, 325 (1996).
- [16] F. Hecht, New development in freefem⁺⁺, *J. Numer. Math.* **20**, 251 (2013).
- [17] U. Ayachit, *The ParaView Guide: A Parallel Visualization Application* (Kitware, Inc., USA, 2015).
- [18] M. Lighthill, On waves generated in dispersive systems by travelling forcing effects, with applications to the dynamics of rotating fluids., *J. Fluid Mech.* **27**, 725 (1967).